CRYSTAL GROWTH & DESIGN

Article

Cite This: Cryst. Growth Des. 2019, 19, 1095−1102

pubs.acs.org/crystal

# Synthesis of Cu-Trimesic Acid/Cu-1,4-Benzenedioic Acid via Microdroplets: Role of Component Compositions

Xiang He and Wei-Ning Wang*

Department of Mechanical and Nuclear Engineering, Virginia Commonwealth University, Richmond, Virginia 23219, United States

**ABSTRACT:** Mixed-linker metal−organic frameworks (MOFs) offer great tunability in both pore structures and surface chemistry. This study reports the synthesis and characterization of model mixed-linker MOFs (i.e., Cu-TMA/Cu-BDC; BDC = 1,4-benzenedioic acid, TMA = trimesic acid) via a microdroplet-based spray process, to unravel the relationship between the properties of mixed-linker MOFs and the component compositions. The as-prepared mixed-linker MOFs exhibited distinct properties in terms of morphology, crystalline phase, surface chemistry, and pore structure. In particular, two-dimensional correlation spectroscopy (2D-COS) analysis was conducted to analyze the correlational features among surface functional groups, which are unattainable from traditional infrared and Raman spectra. The results from the 2D-COS analysis also suggest that the surface chemistry of the mixed-linker MOFs is adjustable by controlling the precursor conditions. Measurements of $CO_2$ adsorption on the mixed-linker MOFs demonstrated the tunability of the preferential adsorption sites and adsorption kinetics. All the above-mentioned information implies that synthetic parameters can be varied to optimize the performance of the mixed-linker MOFs. The outcome of this study offers new insights into the synthetic chemistry of mixed-linker MOFs in a microdroplet-based spray process.

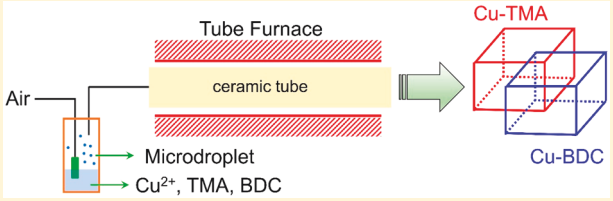


## INTRODUCTION

Metal−organic frameworks (MOFs) have attracted extensive attention during the past few decades due to their unique properties (e.g., high surface area and extraordinary porosity) and great potential in numerous applications (e.g., gas adsorption, catalysis, and sensing).[1,2] Recently, considerable interest has been directed toward synthesizing mixed-component MOFs,[3−7] which provides opportunities to grant the frameworks with more remarkable properties, such as pore heterogeneity,[8,9] framework flexibility,[10] and enhanced selectivity toward gas molecules.[11] The mixed-component MOFs could be multiple-linker MOFs or multiple-metal MOFs, consisting of components either with an identical structure or distinct structures.[8]

Notable examples include hybrid zeolitic imidazolate framework (ZIF) systems, which have been intensively explored for controllable textual properties and sorbate diffusion properties.[10,12,13] For instance, Guo et al. studied the kinetic-controlled formation of $Zn(2\text{-mIM})_2/Co(2\text{-mIM})_2$ (2-mIM = 2-methylimidazole),[12] where sophisticated heterogeneous structures were obtained by manipulating the Co/Zn ratios. Nair and co-workers studied the hybrid ZIF materials (e.g., ZIF-7-8, ZIF-7-90, and ZIF-8-90) synthesized with mixed imidazole linkers (e.g., benzimidazole, 2-mIM, and 2-carboxyimidazole) in the precursor solutions.[10,14−16] With controlled synthesis, they were able to achieve distinct crystalline phases, flexible framework, and tunable pore structures. In addition to the hybrid ZIF systems, other mixed-component MOF systems have also been studied, such as IRMOF systems containing various functionalized linkers,[17] and MIL systems with mixed metals.[18]

Generally, these mixed-component MOFs can be constructed either with a one-pot reaction of multiple components or postsynthetic modification of a single-component MOF.[12] Recently, a microdroplet-based spray process has been developed for the synthesis of MOFs, which has shown several advantages over the conventional methods, such as fast reaction rate and homogeneous distribution of the reactants.[19,20] The attempt to synthesize multicomponent MOFs using the spray process was reported in a prior study,[21] where Zn-MOF-74/Ni-MOF-74 and HKUST-1/NOTT-100 superstructures were fabricated. With multiple components in the precursor microdroplets, the formation mechanism of MOFs would become much more complicated. For instance, it is still unclear, when the microdroplet-based spray process is used, whether the formation of one MOF component would affect the other one and how the properties of the mixed-component MOFs would change with different ratios of individual components.

To make the spray process a better platform for the synthesis of mixed-component MOFs, it is crucial to answer the above-mentioned questions. Therefore, in this article, we carried out a systematic study on the synthesis of a series of mixed-component MOFs with two distinct linkers by using the microdroplet-based spray process. To be specific, two prototypical MOFs, i.e., Cu-TMA (TMA: trimesic acid) and Cu-BDC (BDC: 1,4-benzenedioic acid), were chosen as the components for the mixed-component MOFs. The results

Received: October 25, 2018
Revised: December 3, 2018
Published: December 21, 2018





DOI: 10.1021/acs.cgd.8b01606
Cryst. Growth Des. 2019, 19, 1095−1102

show that the Cu-TMA/Cu-BDC mixed-linker MOFs can be successfully fabricated in a range of compositions as verified by the corresponding X-ray diffraction (XRD) analysis. A variety of other characterizations of the MOFs were also conducted. Especially, two-dimensional correlation spectroscopy (2D-COS) was used to achieve a better spectral resolution and unravel the correlation between the linkers and the properties of the mixed-component MOF over a wide range of compositions, which is unreachable from traditional one-dimensional (1D) infrared (IR) or Raman spectra. The current study also demonstrates that the ratios of the organic linkers could be adjusted to tune the morphologies, surface chemistry, $CO_2$ adsorption capacity, and preferential adsorption site, and achieve hierarchical pore structures. The outcome of this study would constitute a fundamental advance toward the synthetic chemistry of mixed-linker MOFs in the microdroplet-based spray processes.

## MATERIALS AND METHODS

**Synthesis Process.** The synthesis of mixed-linker MOFs by using the microdroplet-based spray process is illustrated in Scheme 1A. To be specific, the precursor solution was prepared by dissolving 0.2174 g of copper nitrate trihydrate, 0.0997 g of 1,4-benzenedioic acid (BDC), and a certain amount of trimesic acid (TMA) in 30 mL of dimethylformamide (DMF). The precursor solution was then atomized to microdroplets, which were subsequently carried by air flow (5 L/min) through an electric furnace at 300 °C, where the solvent evaporates, and the chemicals were converted to final products. A filter was used to collect the sample powders downstream of the furnace. The as-collected samples were dispersed in 10 mL of methanol and precipitated by centrifuging at 6000 rpm for 5 min. This dispersion−centrifugation process was repeated three times in order to remove all the chemical residuals. Finally, the samples were dried in a vacuum oven at 50 °C. On the basis of the amount of the chemicals used in the precursor solution, the as-prepared samples were termed hereafter Cu-TMA (Scheme 1B), Cu-BDC (Scheme 1C), and Cu-$(BDC)_2(TMA)_x$, where the subscripts were used to indicate the mole ratio of the components.

**Scheme 1. Schematic Illustrations of (A) the Synthesis Procedure, (B) the Structure of Cu-TMA and (C) the Structure of Cu-BDC**

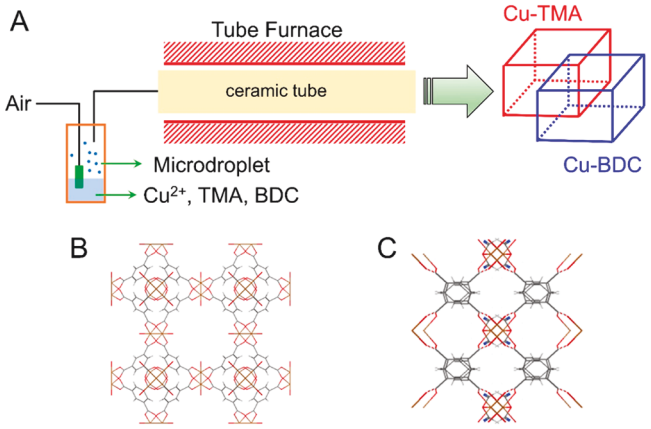


**Material Characterization.** The morphology and crystallinity of the materials were analyzed by scanning electron microscopy (SEM, SU-70, Hitachi) and powder X-ray diffraction (XRD, X'Pert PRO, PANalytical), respectively. The Fourier transform infrared (FTIR) and Raman spectra were obtained by using Nicolet iS50 (Thermo Scientific) and LabRAM HR Evolution (HORIBA), respectively. The surface area and pore size distribution were measured by using Autosorb iQ (Quantachrome Instruments). The elemental composition was determined by using X-ray photoelectron spectroscopy (XPS, ESCALab 250, ThermoFisher). Diffuse reflectance infrared Fourier transform spectroscopy (DRIFTS) was applied to analyze $CO_2$ adsorption behaviors on the as-prepared samples, the procedures of which have been detailed elsewhere.[22]

**Two-Dimensional Correlation Spectroscopy (2D-COS).** 2D-COS method[23] was used to (1) get a better resolution of the spectroscopic peaks and (2) analyze correlational features among chemical groups. The fundamentals and computation procedures of the 2D-COS have been detailed elsewhere.[23] In this work, the 2Dshige software developed by Kwansei-Gakuin University was used to generate two 2D correlation spectra (i.e., the synchronous spectrum and the asynchronous spectrum).

## RESULTS AND DISCUSSION

**Material Characterization.** The morphologies of Cu-BDC, Cu-TMA, and Cu-$(BDC)_2(TMA)_x$ were examined by SEM. As shown in Figure 1A, the pure Cu-TMA sample has a spherical shape, which can be attributed to the typical formation mechanism in the spray process,[19,24] while with an

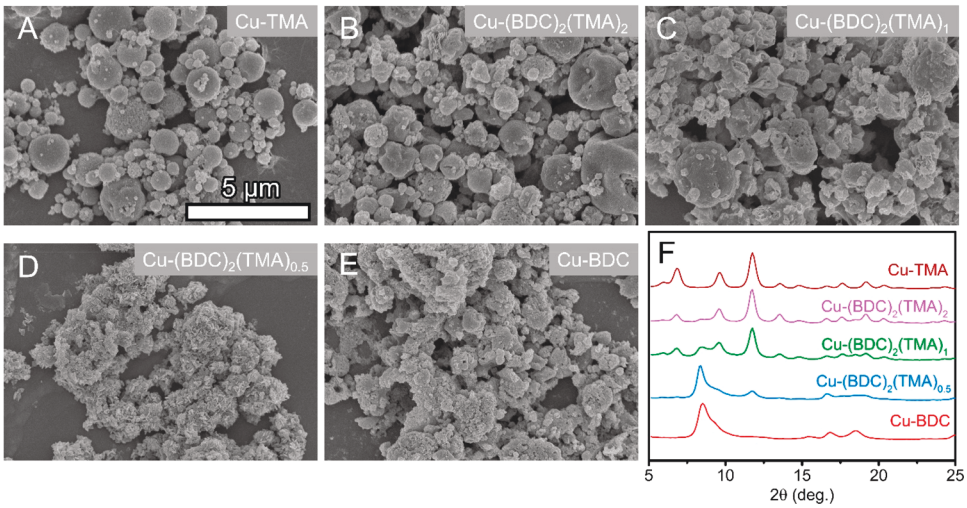


**Figure 1.** SEM images of the samples: (A) Cu-TMA; (B) Cu-$(BDC)_2(TMA)_2$; (C) Cu-$(BDC)_2(TMA)_1$; (D) Cu-$(BDC)_2(TMA)_{0.5}$; (E) Cu-BDC; (F) XRD patterns of the samples.



DOI: 10.1021/acs.cgd.8b01606
Cryst. Growth Des. 2019, 19, 1095−1102

increasing amount of BDC the spherical shape of the samples became less intact (Figure 1B–E). The crystal structures of the samples were analyzed with XRD measurements. As shown in Figure 1F, the diffraction patterns of both Cu-BDC and Cu-TMA agree well with the previously reported ones.[19,25] For Cu-$(BDC)_2(TMA)_x$, the characteristic diffraction peaks of both MOF components (i.e., Cu-BDC and Cu-TMA) can be clearly identified, indicating the coexistence of both MOFs. The intensity ratios of these characteristic peaks were found to be dependent on the relative amount of the MOF components. On the basis of the XRD patterns, the weight percentages of the MOF components in Cu-$(BDC)_2(TMA)_x$ were analyzed with the Rietveld confinement using the MAUD program (MAUD: Materials Analysis Using Diffraction). After the confinement, the weight percentages of Cu-TMA in Cu-$(BDC)_2(TMA)_2$, Cu-$(BDC)_2(TMA)_1$, and Cu-$(BDC)_2(TMA)_{0.5}$ were calculated to be 78.9, 54.5, and 5.4 wt %, respectively. Notably, the actual ratios of the components in the products slightly deviated from those of the precursors, which might be related to the variations in crystallization rates between Cu-TMA and Cu-BDC.

The surface functional groups of the Cu-$(BDC)_2(TMA)_x$ samples were analyzed by FTIR (Figure 2A), where the

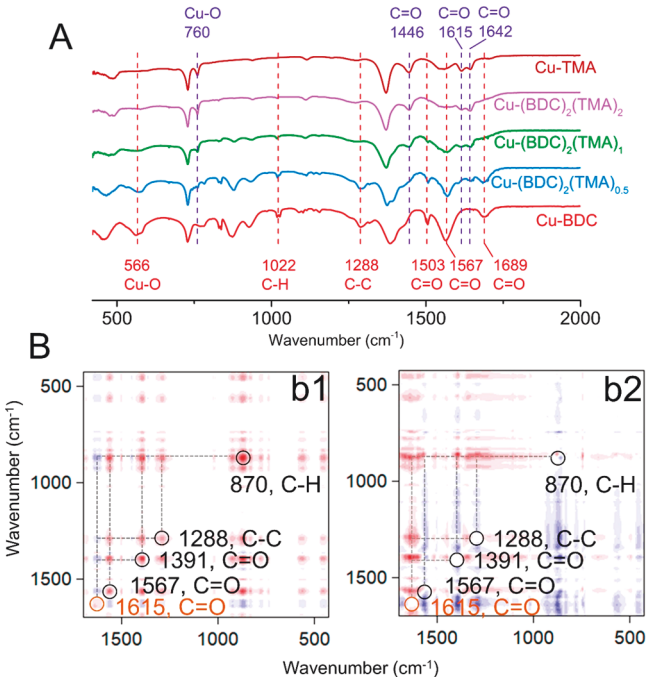


**Figure 2.** (A) Traditional 1D FT-IR spectra of the samples (top: functional groups in Cu-TMA, bottom: functional groups in Cu-BDC); (B) 2D FT-IR correlation spectra with decreasing amount of TMA in precursors as the perturbation: (b1) synchronous and (b2) asynchronous.

characteristic peaks of individual MOF can be clearly observed. For instance, Cu-TMA has several characteristic peaks at 760 and 1446 $cm^{-1}$, corresponding to Cu–O[26] and C═O,[27] respectively. In addition, both peaks at 1615 and 1642 $cm^{-1}$ can be ascribed to C═O,[19,28,29] originating from the carboxyl group in TMA coordinated with the Cu sites. On the other hand, Cu-BDC has several characteristic peaks at 566, 1022, and 1288 $cm^{-1}$, which can be assigned to Cu–O,[30] C–H,[31,32] and C–C,[33] respectively. The peaks at 1503, 1567, and 1689 $cm^{-1}$ are related to C═O in BDC.[28,34,35] It is interesting to note that the relative intensities of these characteristic IR peaks change with different ratios of Cu-BDC to Cu-TMA. Unfortunately, little information regarding correlational features of these IR peaks can be obtained from the conventional 1D FT-IR spectra.

To get better resolved peaks and correlational features of the IR peaks, the 2D-COS method was used to generate 2D FTIR correlation spectra with a decreasing amount of TMA in precursors as the perturbation. The 2D FTIR correlation spectra consist of a synchronous spectrum (Figure 2b1) and an asynchronous spectrum (Figure 2b2), which can be used to analyze the dynamic spectral fluctuations (e.g., increase or decrease of peak intensity) and sequential orders of the variations of the IR peaks, respectively (see Table 1 for details).[36] In particular, the synchronous spectrum is symmetrical with respect to the diagonal line, where several peaks are located (Figure 2b1). These peaks are called autopeaks, the intensity of which indicates the extent of the fluctuations of a peak at a specific wavenumber. As shown in Figure 2b1, five dominant autopeaks, indicated by red color, are observed at 870 $cm^{-1}$ (C–H), 1288 $cm^{-1}$ (C–C), 1391 $cm^{-1}$ (C═O), 1567 $cm^{-1}$ (C═O), and 1615 $cm^{-1}$ (C═O), suggesting that the intensity changes of these peaks were much greater than others (e.g., 566 $cm^{-1}$ (Cu–O)) and the variations in the precursor linkers would mainly lead to the changes in surface chemistry of the mixed-component MOFs. The peaks off the diagonal line are referred to as cross peaks, the color of which represents the trends of the fluctuations (Table 1). Notably, the cross peaks at (1615, Y) (Y = 870, 1288, 1391, 1567 $cm^{-1}$) exhibit blue color, which means that the intensity of the band at 1615 $cm^{-1}$ (i.e., C═O in TMA) changes in the opposite direction of the other bands (i.e., 870, 1288, 1391, 1567 $cm^{-1}$, corresponding to functional groups in BDC).

Unlike the synchronous spectrum, the asynchronous spectrum has no peaks on the diagonal line (i.e., no autopeaks), while the asynchronous spectrum contains similar cross peaks off the diagonal line as the synchronous one. By comparing the colors of the same cross peaks in both synchronous and asynchronous spectra, the sequential orders of the spectral variations can be obtained.[36] To be specific, if the cross peak (X, Y) shows the same color in synchronous and asynchronous spectra, then the IR band at X $cm^{-1}$ changes before that at Y $cm^{-1}$. Otherwise, the IR band at X $cm^{-1}$

**Table 1. Guidelines of 2D-COS Analysis**

| 2D COS analysis | | |
|---|---|---|
| | synchronous | asynchronous |
| autopeaks (i.e., peaks on the diagonal line) | extent of the spectral fluctuations[a] | N/A |
| cross peaks (i.e., peaks off the diagonal line) | trends of the fluctuations[b] | sequential orders of the spectral variations[c] |

[a]Stronger color indicates a higher extent of the spectral fluctuation. [b]Red cross peak (X, Y) indicates that the bands at X $cm^{-1}$ and Y $cm^{-1}$ change in the same direction. Otherwise (i.e., blue cross peak), these bands change in the opposite direction. [c]If a cross peak (X, Y) shows the same color in both synchronous and asynchronous spectra, this implies that the band at X $cm^{-1}$ changes before that at Y $cm^{-1}$. Otherwise, the band at X $cm^{-1}$ changes after that at Y $cm^{-1}$. Special case: cross peak (X, Y) in either spectrum has no color: bands at X and Y $cm^{-1}$ change simultaneously.


DOI: 10.1021/acs.cgd.8b01606
Cryst. Growth Des. 2019, 19, 1095–1102

changes after that at Y $cm^{-1}$. One special case is that, if the cross peak (X, Y) in either spectrum has no color, the IR bands at X and Y $cm^{-1}$ change simultaneously.[37] With a decreasing amount of TMA in precursors, the changes of the spectral peaks occurred in the following sequence: 1288 $cm^{-1}$ (C−C in BDC) = 1391 $cm^{-1}$ (C═O in BDC) > 1567 $cm^{-1}$ (C═O in BDC) > 870 $cm^{-1}$ (C−H in BDC) > 1615 $cm^{-1}$ (C═O in TMA). Interestingly, some peaks originate from BDC, but they do not change synchronously. This implies that mutual effects exist during the simultaneous synthesis of multiple MOFs in microdroplets, and the surface chemistry of individual MOF component could be finely tuned by changing the precursor composition.

The vibration properties of the samples were further analyzed with the aid of Raman spectroscopy, which is complementary to IR spectroscopy, aiming to uncover a complete picture of surface chemistry of the samples. As shown in Figure 3A, both Cu-TMA and Cu-BDC have several

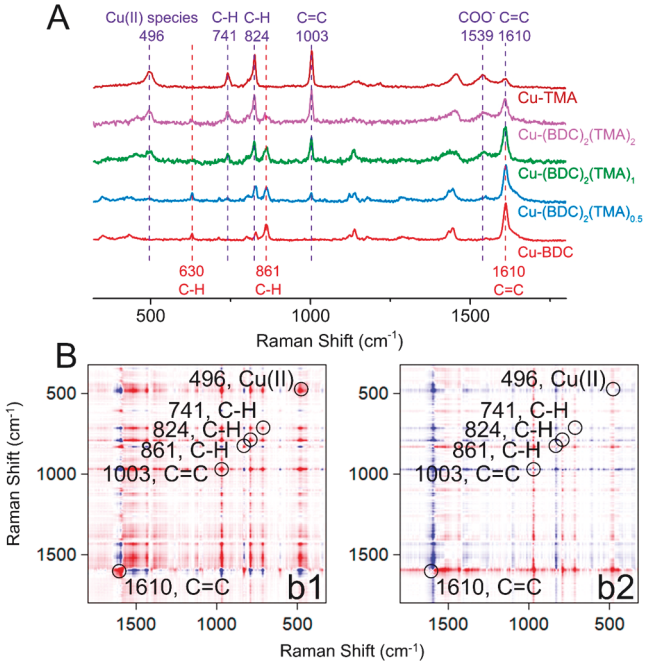


**Figure 3.** (A) Traditional 1D Raman spectra of the samples (top: functional groups in Cu-TMA, bottom: functional groups in Cu-BDC); (B) 2D Raman correlation spectra with decreasing amount of TMA in precursors as the perturbation: (b1) synchronous and (b2) asynchronous.

characteristic peaks. For Cu-TMA, several peaks were observed at 496 $cm^{-1}$, 741 $cm^{-1}$, 824 $cm^{-1}$, 1003 $cm^{-1}$, 1539 and 1610 $cm^{-1}$. In particular, the peak at 496 $cm^{-1}$ originates from Cu(II) species.[38] The peaks at 741 and 824 $cm^{-1}$ can be attributed to the vibration of the C−H group,[39] while the peaks at 1003 and 1610 $cm^{-1}$ are related to the vibration of the C═C group.[39] The band at 1539 $cm^{-1}$ is due to the vibration of $COO^-$.[40] In the case of Cu-BDC, the peaks at 630 and 861 $cm^{-1}$ can be assigned to C−H in BDC.[41] Additionally, the peak at 1610 $cm^{-1}$ is also observed but with a much higher intensity for the case of Cu-BDC, which is associated with the C═C in BDC.[42] Similar to the FTIR results, the intensities of these Raman peaks also varied with the composition of the MOF mixtures.

To get further information regarding the mutual effects of MOFs mixtures during the synthesis process, the same 2D-COS approach was employed to deconvolute the 1D Raman spectra into 2D correlation ones with a decreasing amount of TMA in precursors as the perturbation. The guidelines (Table 1) used to analyze 2D FTIR spectra also apply here. As shown in Figure 3A, six autopeaks were observed in the synchronous spectrum, including 496 $cm^{-1}$ (Cu(II) species), 741 $cm^{-1}$ (C−H), 824 $cm^{-1}$ (C−H), 861 $cm^{-1}$ (C−H), 1003 $cm^{-1}$ (C═C), and 1610 $cm^{-1}$ (C═C). As shown from the color of the cross peaks, with a decreasing amount of TMA in the precursor, the intensities of Raman peaks at 861 $cm^{-1}$ (C−H in BDC) and 1610 $cm^{-1}$ (C═C in TMA/BDC) change in the opposite direction of the rest peaks (i.e., functional groups in TMA). From the information on the cross peaks in both synchronous spectrum and asynchronous spectrum, the sequence of the spectral variations was derived as follows: 824 $cm^{-1}$ (C−H in TMA) > 741 $cm^{-1}$ (C−H in TMA) = 496 $cm^{-1}$ (Cu(II) species in Cu-TMA) > 1003 $cm^{-1}$ (C═C in TMA) > 1610 $cm^{-1}$ (C═C in TMA/BDC) > 861 $cm^{-1}$ (C−H in BDC). As shown, the spectral fluctuations occurred with different sequential orders even for functional groups from the same component, which agrees with the FTIR results, once again demonstrating the tunability of the surface chemistry of individual MOF component with various linker compositions. Besides, the information on the sequential orders offers clues for the interactions between the mixed components and provides evidence for the framework interpenetration. It would also be of great importance to guide us in designing mixed-component MOFs with specified surface chemistries for future applications.

The porosities and surface areas of the as-prepared samples were analyzed by nitrogen sorption measurements. The nitrogen sorption isotherms and pore size distributions are shown in Figure 4, and the deduced values were summarized in

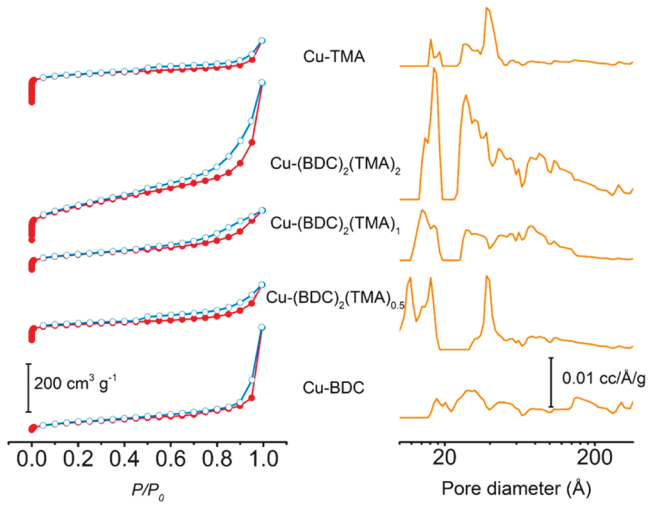


**Figure 4.** Left: nitrogen sorption isotherms; right: pore size distribution calculated using density functional theory (DFT).

Table 2. As shown in Figure 4, Cu-BDC demonstrates type IV nitrogen sorption isotherm, indicating the dominance of mesopores, which is in line with the corresponding pore size distribution. The Brunauer−Emmett−Teller (BET) surface area and pore volume of Cu-BDC were found to be 121 $m^2/g$ and 0.40 $cm^3/g$, respectively. On the other hand, Cu-TMA


DOI: 10.1021/acs.cgd.8b01606
Cryst. Growth Des. 2019, 19, 1095−1102

**Table 2. Summary of BET Surface Areas and Pore Volumes**

| samples | BET surface area ($m^2/g$) | pore volume ($cm^3/g$) |
|---|---|---|
| Cu-TMA | 763 | 0.43 |
| Cu-$(BDC)_2(TMA)_2$ | 657 | 0.88 |
| Cu-$(BDC)_2(TMA)_1$ | 300 | 0.37 |
| Cu-$(BDC)_2(TMA)_{0.5}$ | 348 | 0.33 |
| Cu-BDC | 121 | 0.40 |

exhibits type I isotherm with massive micropores. The slight rise and the hysteresis loop observed at high relative pressure implies the existence of mesopores, which is attributed to the interparticle voids.[43] The as-synthesized Cu-TMA has a BET surface area of 763 $m^2/g$ and a pore volume of 0.43 $cm^3/g$. Notably, hierarchical pore structures (i.e., micromesopores) were found in the cases of Cu-$(BDC)_2(TMA)_x$ samples. To be specific, the nitrogen sorption isotherms of Cu-$(BDC)_2(TMA)_x$ samples feature sharp nitrogen uptake at low relative pressure ($P/P_0 < 0.01$), and an obvious rise and a hysteresis loop at high relative pressures ($P/P_0 > 0.5$), suggesting the coexistence of abundant micropores and mesopores. This hierarchical pore structures can accelerate mass transfer rates and thus facilitates the overall efficiency of practical applications, such as catalysis.[44] Moreover, the BET surface areas and pore volumes of the Cu-$(BDC)_2(TMA)_x$ samples also have a great dependence on the ratio of BDC to TMA used in the precursor solution. Overall, the BET surface area decreases with a decreasing amount of TMA in the mixed-component MOFs. Interestingly, the highest pore volume was found with Cu-$(BDC)_2(TMA)_2$ (i.e., 0.88 $cm^3/g$), which might be attributed to formation of additional pores due to the framework interpenetration.[45]

The variations in surface elemental composition among these samples were analyzed by using XPS, which can provide further information regarding synthetic chemistry of mixed-linker MOFs in microdroplets. As shown in Figure 5A, analogous survey scans were observed for these samples, where the main elements could be clearly identified, including Cu, N, and O. High-resolution spectra of these elements are shown in Figure 5B–D. The presence of N is due to the existence of DMF residues in the pore channels or coordinated DMF at the Cu sites (Figure 5B). For Cu-TMA, a small amount of N was observed, indicating the limited ability of methanol to exchange DMF from the framework, which might be ascribed to the limitation from the micropore structures. In contrast, no peak was observed at 398.2 eV in the case of Cu-BDC (Figure 5B), suggesting the absence of DMF in the as-prepared Cu-BDC crystals. Interestingly, higher N peaks were observed in the case of mixed-linker MOFs, which implies a higher amount of DMF existing in the mixed-linker MOFs, which might be owing to the interpenetrating framework preventing the release of DMF molecules.[46] Typically, DMF molecules exist inside the framework through the coordination with metal sites. The release of DMF molecules from the framework would give rise to coordinatively unsaturated metal sites and enhanced porosity, which are beneficial for several applications, including catalysis and gas storage.[47] On the other hand, the coordination of DMF molecules with Cu sites is necessary to maintain the structural integrity of some MOFs, like Cu-BDC.[25] Therefore, as a trade-off between functionality and structural integrity, careful considerations are always required about the presence of DMF inside the framework. In addition, the samples also exhibit variations in the valence states of Cu due to the coordination with distinct linkers and different amounts of DMF molecules. As shown in the high-resolution XPS spectra of Cu 2p (Figure 5C), both Cu-TMA and Cu-BDC display peaks at 932.8 and 952.5 eV, corresponding to Cu $2p_{3/2}$ and Cu $2p_{1/2}$, respectively.[48,49] In addition, for Cu-BDC, satellite peaks were observed at 931.1 and 950.9 eV. The peak intensities of Cu 2p vary with different component

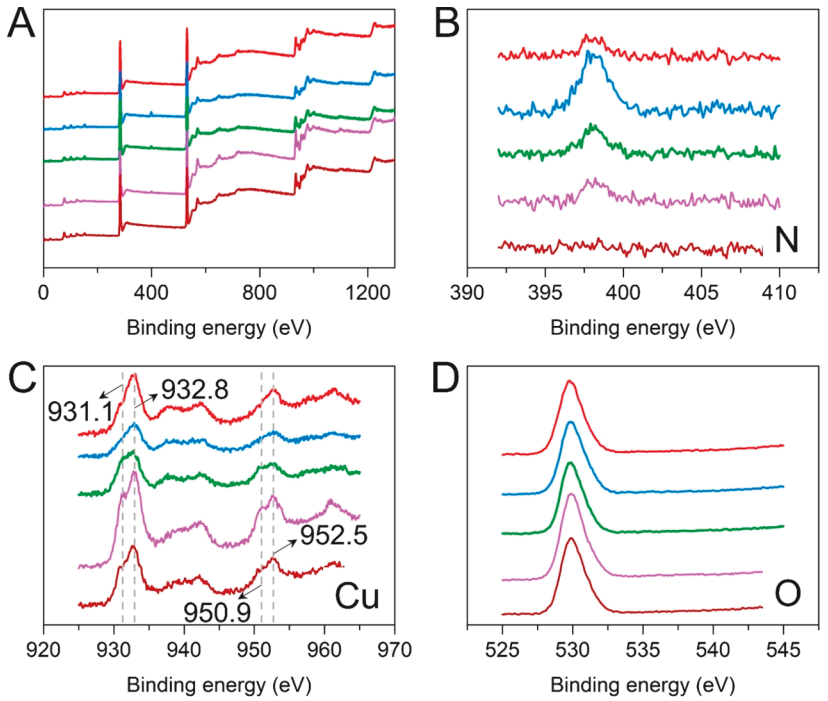


**Figure 5.** XPS spectra: (A) survey scan; (B) N 1s; (C) Cu 2p; (D) O 1s (from top to bottom: Cu-TMA, Cu-$(BDC)_2(TMA)_2$, Cu-$(BDC)_2(TMA)_1$, Cu-$(BDC)_2(TMA)_{0.5}$, and Cu-BDC).



DOI: 10.1021/acs.cgd.8b01606
Cryst. Growth Des. 2019, 19, 1095–1102

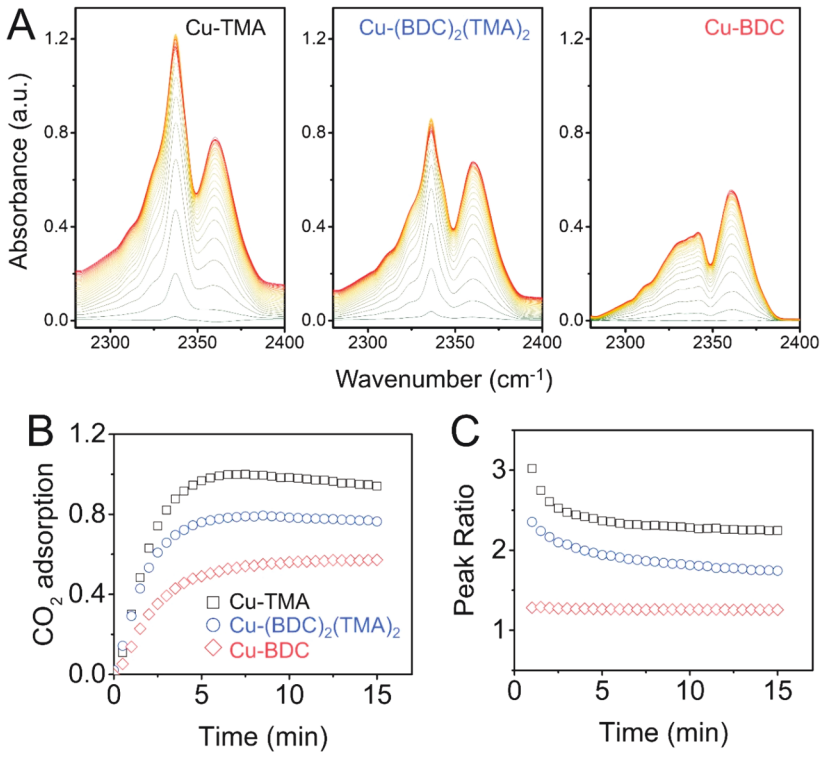


**Figure 6.** (A) In situ IR spectra collected during the 15 min $CO_2$ adsorption process; (B) $CO_2$ adsorption kinetics; (C) area ratios of peak (2337 $cm^{-1}$) to peak (2360 $cm^{-1}$) as a function of adsorption time.

compositions. Interestingly, the intensity changes of Cu 2p peak followed the opposite trend of those of N 1s (Figure 5B), suggesting the peak intensity of Cu 2p was closely related to the amount of DMF remaining in the framework. In other words, with more DMF molecules remaining in the framework, less signal from Cu 2p would be detected during the XPS measurements. This is reasonable, as XPS only detects photoemitted electrons escaped from the samples, while the presence of DMF molecules could block electrons emitted from Cu 2p from escaping and reaching the XPS detector. On the other hand, no apparent differences were observed in the high-resolution XPS spectra of O 1s (Figure 5D).

In addition to property characterization, the gas adsorption performance of the as-prepared MOFs was also evaluated. In particular, DRIFTS was used to analyze the $CO_2$ adsorption behaviors of these samples. As shown in Figure 6A, the characteristic IR peaks of adsorbed $CO_2$ on three representative samples have different areas and shapes, indicating the various $CO_2$ adsorption capacity and preferential sites. Specifically, the IR peak area is closely related to the amount of adsorbed $CO_2$ molecules. Therefore, the peak areas in the wavenumber range from 2220 to 2450 $cm^{-1}$ were measured as a function of time and then used to obtain the $CO_2$ adsorption kinetics (Figure 6B). As exhibited in Figure 6B, Cu-TMA shows the highest $CO_2$ adsorption rate and capacity, followed by Cu-$(BDC)_2(TMA)_2$ and then Cu-BDC. Moreover, the adsorbed $CO_2$ exhibits two IR bands at 2337 and 2360 $cm^{-1}$ (Figure 6A), corresponding to the interaction of $CO_2$ molecules with metal sites and functional groups, respectively.[19] Interestingly, with more Cu-TMA, the intensity of peak (2337 $cm^{-1}$) becomes larger while the intensity of peak (2360 $cm^{-1}$) becomes smaller, inferring the changes in the preferential adsorption of $CO_2$ molecules on the sites of copper ions over functional groups. To quantify the preferential adsorption, the area ratios of the IR peak (2337 $cm^{-1}$) to peak (2360 $cm^{-1}$) were calculated and presented in Figure 6C. For the case of pure Cu-TMA, the peak ratio had the highest value (i.e., 3.02) in the beginning of the adsorption process, and then gradually decreased and stabilized at 2.25, indicating that $CO_2$ molecules prefer to be adsorbed with the interaction with metal sites, and then on the functional groups, while, in the case of Cu-BDC, the values of the peak ratios were the lowest but also the most stable ones, suggesting that there is no variation in the preferential adsorption site during the evolution process. The above results imply that both preferential adsorption site and adsorption capacity of $CO_2$ molecules are tunable by adjusting the component ratios in the mixed-linker MOFs.

## CONCLUSION

In summary, Cu-TMA/Cu-BDC mixed-linker MOFs with a range of component ratios have been successfully fabricated via the microdroplet-based spray process. Results show that the adjustment of the mole ratio of TMA to BDC in the precursor solution would allow continuous tuning of the properties of mixed-linker MOFs, including crystalline phases, surface chemistry, and textual properties. In particular, the mixed-linker MOFs possess an interpenetrating framework, which leads to the formation of additional pores and thus increased pore volume. Moreover, DRIFTS was also used to study the $CO_2$ preferential adsorption sites and adsorption kinetics, which have also been proven to have significant dependence on the component ratios of mixed-linker MOFs. This is the first systematic study of the synthetic chemistry of mixed-linker MOFs in the microdroplet-based spray process. It is expected that, through rational control of the synthetic parameters, the microdroplet-based spray process can be applied to produce a


DOI: 10.1021/acs.cgd.8b01606
Cryst. Growth Des. 2019, 19, 1095−1102

variety of mixed-component MOFs with specifically desired properties.

## AUTHOR INFORMATION


### Corresponding Author

*Tel: 1-(804) 827-4306; fax: 1-(804) 827-7030; e-mail: wnwang@vcu.edu.

### ORCID

Wei-Ning Wang: 0000-0002-1935-6301


### Notes

The authors declare no competing financial interest.

## ACKNOWLEDGMENTS

This work is supported by the National Science Foundation (CMMI-1727553).

## REFERENCES


(1) Yuan, S.; Feng, L.; Wang, K.; Pang, J.; Bosch, M.; Lollar, C.; Sun, Y.; Qin, J.; Yang, X.; Zhang, P.; Wang, Q.; Zou, L.; Zhang, Y.; Zhang, L.; Fang, Y.; Li, J.; Zhou, H. C. Stable Metal-Organic Frameworks: Design, Synthesis, and Applications. *Adv. Mater.* **2018**, *30*, 1704303.

(2) Wang, S.; Wang, X. Multifunctional Metal−Organic Frameworks for Photocatalysis. *Small* **2015**, *11*, 3097−3112.

(3) Bunck, D. N.; Dichtel, W. R. Mixed Linker Strategies for Organic Framework Functionalization. *Chem. - Eur. J.* **2013**, *19*, 818−827.

(4) Dhakshinamoorthy, A.; Asiri, A. M.; Garcia, H. Mixed-Metal or Mixed-linker Metal Organic Frameworks as Heterogeneous Catalysts. *Catal. Sci. Technol.* **2016**, *6*, 5238−5261.

(5) Tanasaro, T.; Adpakpang, K.; Ittisanronnachai, S.; Faungnawakij, K.; Butburee, T.; Wannapaiboon, S.; Ogawa, M.; Bureekaew, S. Control of Polymorphism of Metal−Organic Frameworks Using Mixed-Metal Approach. *Cryst. Growth Des.* **2018**, *18*, 16−21.

(6) Zhai, Z.-W.; Yang, S.-H.; Cao, M.; Li, L.-K.; Du, C.-X.; Zang, S.-Q. Rational Design of Three Two-Fold Interpenetrated Metal−Organic Frameworks: Luminescent Zn/Cd-Metal−Organic Frameworks for Detection of 2,4,6-Trinitrophenol and Nitrofurazone in the Aqueous Phase. *Cryst. Growth Des.* **2018**, *18*, 7173−7182.

(7) Rachuri, Y.; Parmar, B.; Suresh, E. Three-Dimensional Co(II)/Cd(II) Metal−Organic Frameworks: Luminescent Cd-MOF for Detection and Adsorption of 2,4,6-Trinitrophenol in the Aqueous Phase. *Cryst. Growth Des.* **2018**, *18*, 3062−3072.

(8) Lee, S. J.; Doussot, C.; Baux, A.; Liu, L.; Jameson, G. B.; Richardson, C.; Pak, J. J.; Trousselet, F.; Coudert, F.-X.; Telfer, S. G. Multicomponent Metal−Organic Frameworks as Defect-Tolerant Materials. *Chem. Mater.* **2016**, *28*, 368−375.

(9) Koh, K.; Wong-Foy, A. G.; Matzger, A. J. MOF@MOF: Microporous Core-Shell Architectures. *Chem. Commun.* **2009**, 6162−6164.

(10) Rashidi, F.; Blad, C. R.; Jones, C. W.; Nair, S. Synthesis, Characterization, and Tunable Adsorption and Diffusion Properties of Hybrid ZIF-7−90 Frameworks. *AIChE J.* **2016**, *62*, 525−537.

(11) Burrows, A. D. Mixed-Component Metal-Organic Frameworks (MC-MOFs): Enhancing Functionality Through Solid Solution Formation and Surface Modifications. *CrystEngComm* **2011**, *13*, 3623−3642.

(12) Guo, W.; Xia, W.; Cai, K.; Wu, Y.; Qiu, B.; Liang, Z.; Qu, C.; Zou, R. Kinetic-Controlled Formation of Bimetallic Metal−Organic Framework Hybrid Structures. *Small* **2017**, *13*, 1702049.

(13) Wu, T.; Bu, X.; Zhang, J.; Feng, P. New Zeolitic Imidazolate Frameworks: From Unprecedented Assembly of Cubic Clusters to Ordered Cooperative Organization of Complementary Ligands. *Chem. Mater.* **2008**, *20*, 7377−7382.

(14) Thompson, J. A.; Blad, C. R.; Brunelli, N. A.; Lydon, M. E.; Lively, R. P.; Jones, C. W.; Nair, S. Hybrid Zeolitic Imidazolate Frameworks: Controlling Framework Porosity and Functionality by Mixed-Linker Synthesis. *Chem. Mater.* **2012**, *24*, 1930−1936.

(15) Thompson, J. A.; Brunelli, N. A.; Lively, R. P.; Johnson, J. R.; Jones, C. W.; Nair, S. Tunable $CO_2$ Adsorbents by Mixed-Linker Synthesis and Postsynthetic Modification of Zeolitic Imidazolate Frameworks. *J. Phys. Chem. C* **2013**, *117*, 8198−8207.

(16) Eum, K.; Jayachandrababu, K. C.; Rashidi, F.; Zhang, K.; Leisen, J.; Graham, S.; Lively, R. P.; Chance, R. R.; Sholl, D. S.; Jones, C. W.; Nair, S. Highly Tunable Molecular Sieving and Adsorption Properties of Mixed-Linker Zeolitic Imidazolate Frameworks. *J. Am. Chem. Soc.* **2015**, *137*, 4191−4197.

(17) Deng, H.; Doonan, C. J.; Furukawa, H.; Ferreira, R. B.; Towne, J.; Knobler, C. B.; Wang, B.; Yaghi, O. M. Multiple Functional Groups of Varying Ratios in Metal-Organic Frameworks. *Science* **2010**, *327*, 846−850.

(18) Serre, C.; Millange, F.; Thouvenot, C.; Gardant, N.; Pellé, F.; Férey, G. Synthesis, Characterisation and Luminescent Properties of a New Three-Dimensional Lanthanide Trimesate: $M((C_6H_3)-(CO_2)_3)$ (M = Y, Ln) or MIL-78. *J. Mater. Chem.* **2004**, *14*, 1540−1543.

(19) He, X.; Gan, Z.; Fisenko, S.; Wang, D.; El-Kaderi, H. M.; Wang, W.-N. Rapid Formation of Metal−Organic Frameworks (MOFs) Based Nanocomposites in Microdroplets and Their Applications for $CO_2$ Photoreduction. *ACS Appl. Mater. Interfaces* **2017**, *9*, 9688−9698.

(20) Wang, Z.; Ananias, D.; Carné-Sánchez, A.; Brites, C. D. S.; Imaz, I.; Maspoch, D.; Rocha, J.; Carlos, L. D. Lanthanide−Organic Framework Nanothermometers Prepared by Spray-Drying. *Adv. Funct. Mater.* **2015**, *25*, 2824−2830.

(21) Carné-Sánchez, A.; Imaz, I.; Cano-Sarabia, M.; Maspoch, D. A Spray-Drying Strategy for Synthesis of Nanoscale Metal−Organic Frameworks and Their Assembly into Hollow Superstructures. *Nat. Chem.* **2013**, *5*, 203−211.

(22) He, X.; Yang, C.; Wang, D.; Gilliland, S. E., III; Chen, D.-R.; Wang, W.-N. Facile Synthesis of ZnO@ZIF Core-Shell Nanofibers: Crystal Growth and Gas Adsorption. *CrystEngComm* **2017**, *19*, 2445−2450.

(23) Noda, I.; Ozaki, Y. *Two-Dimensional Correlation Spectroscopy: Applications in Vibrational and Optical Spectroscopy*; John Wiley & Sons, 2005.

(24) He, X.; Wang, W.-N. Rational Design of Efficient Semiconductor-based Photocatalysts via Microdroplets: A Review. *KONA Powder Part. J.* **2019**, *36*, 201−214.

(25) Carson, C. G.; Hardcastle, K.; Schwartz, J.; Liu, X.; Hoffmann, C.; Gerhardt, R. A.; Tannenbaum, R. Synthesis and Structure Characterization of Copper Terephthalate Metal−Organic Frameworks. *Eur. J. Inorg. Chem.* **2009**, *2009*, 2338−2343.

(26) Zhang, H.; Xiao, R.; Song, M.; Shen, D.; Liu, J. Hydrogen Production From Bio-Oil by Chemical Looping Reforming. *J. Therm. Anal. Calorim.* **2014**, *115*, 1921−1927.

(27) Kaur, R.; Kaur, A.; Umar, A.; Anderson, W. A.; Kansal, S. K. Metal Organic Framework (MOF) Porous Octahedral Nanocrystals of Cu-BTC: Synthesis, Properties and Enhanced Adsorption Properties. *Mater. Res. Bull.* **2019**, *109*, 124−133.

(28) Huang, K.; Xu, Y.; Wang, L.; Wu, D. Heterogeneous Catalytic Wet Peroxide Oxidation of Simulated Phenol Wastewater by Copper Metal−Organic Frameworks. *RSC Adv.* **2015**, *5*, 32795−32803.

(29) Peng, L.; Wu, S.; Yang, X.; Hu, J.; Fu, X.; Li, M.; Bai, L.; Huo, Q.; Guan, J. Oxidation of Benzyl Alcohol Over Metal Organic Frameworks M-BTC (M = Co, Cu, Fe). *New J. Chem.* **2017**, *41*, 2891−2894.

(30) Kajita, Y.; Arii, H.; Saito, T.; Saito, Y.; Nagatomo, S.; Kitagawa, T.; Funahashi, Y.; Ozawa, T.; Masuda, H. Syntheses, Characterization, and Dioxygen Reactivities of Cu(I) Complexes with cis,cis-1,3,5-Triaminocyclohexane Derivatives: A $Cu(III)_2O_2$ Intermediate Exhibiting Higher C−H Activation. *Inorg. Chem.* **2007**, *46*, 3322−3335.

(31) Münch, A. S.; Lohse, M. S.; Hausdorf, S.; Schreiber, G.; Zacher, D.; Fischer, R. A.; Mertens, F. O. R. L. Room Temperature Preparation Method for Thin MOF-5 Films on Metal and Fused Silica Surfaces using the Controlled SBU Approach. *Microporous Mesoporous Mater.* **2012**, *159*, 132−138.




DOI: 10.1021/acs.cgd.8b01606
*Cryst. Growth Des.* 2019, 19, 1095−1102

(32) Mateo-Martí, E.; Welte, L.; Amo-Ochoa, P.; Sanz Miguel, P. J.; Gómez-Herrero, J.; Martín-Gago, J. A.; Zamora, F. Direct Evidence of Nanowires Formation From a Cu(i) Coordination Polymer. *Chem. Commun.* **2008**, 945−947.
(33) Nijem, N.; Wu, H.; Canepa, P.; Marti, A.; Balkus, K. J.; Thonhauser, T.; Li, J.; Chabal, Y. J. Tuning the Gate Opening Pressure of Metal−Organic Frameworks (MOFs) for the Selective Separation of Hydrocarbons. *J. Am. Chem. Soc.* **2012**, *134*, 15201−15204.
(34) Abid, H. R.; Rada, Z. H.; Shang, J.; Wang, S. Synthesis, Characterization, and $CO_2$ Adsorption of Three Metal-Organic Frameworks (MOFs): MIL-53, MIL-96, and Amino-MIL-53. *Polyhedron* **2016**, *120*, 103−111.
(35) Chen, M.; Gan, N.; Zhou, Y.; Li, T.; Xu, Q.; Cao, Y.; Chen, Y. A Novel Aptamer- Metal Ions- Nanoscale MOF Based Electrochemical Biocodes for Multiple Antibiotics Detection and Signal Amplification. *Sens. Actuators, B* **2017**, *242*, 1201−1209.
(36) Noda, I. Generalized Two-Dimensional Correlation Method Applicable to Infrared, Raman, and other Types of Spectroscopy. *Appl. Spectrosc.* **1993**, *47*, 1329−1336.
(37) Yu, Z.; Zhou, Z.; Huang, G.; Zheng, X.; Wu, L.; Zhao, S.; Meng, F. Two-Dimensional FTIR Spectroscopic Characterization of Functional Groups of NaOCl-Exposed Alginate: Insights into Membrane Refouling after Online Chemical Cleaning. *ACS Appl. Bio Mater.* **2018**, *1*, 593−603.
(38) Ethiraj, J.; Bonino, F.; Lamberti, C.; Bordiga, S. $H_2S$ Interaction with HKUST-1 and ZIF-8 MOFs: A Multitechnique Study. *Microporous Mesoporous Mater.* **2015**, *207*, 90−94.
(39) Prestipino, C.; Regli, L.; Vitillo, J. G.; Bonino, F.; Damin, A.; Lamberti, C.; Zecchina, A.; Solari, P. L.; Kongshaug, K. O.; Bordiga, S. Local Structure of Framework Cu(II) in HKUST-1 Metallorganic Framework: Spectroscopic Characterization upon Activation and Interaction with Adsorbates. *Chem. Mater.* **2006**, *18*, 1337−1346.
(40) Chen, Y.; Wang, H.; Li, J.; Lockard, J. V. *In situ* Spectroscopy Studies of $CO_2$ Adsorption in a Dually Functionalized Microporous Metal−Organic Framework. *J. Mater. Chem. A* **2015**, *3*, 4945−4953.
(41) Bordiga, S.; Lamberti, C.; Ricchiardi, G.; Regli, L.; Bonino, F.; Damin, A.; Lillerud, K. P.; Bjorgen, M.; Zecchina, A. Electronic and Vibrational Properties of a MOF-5 Metal−Organic Framework: ZnO Quantum Dot Behaviour. *Chem. Commun.* **2004**, 2300−2301.
(42) Tan, K.; Nijem, N.; Canepa, P.; Gong, Q.; Li, J.; Thonhauser, T.; Chabal, Y. J. Stability and Hydrolyzation of Metal Organic Frameworks with Paddle-Wheel SBUs upon Hydration. *Chem. Mater.* **2012**, *24*, 3153−3167.
(43) Chaikittisilp, W.; Hu, M.; Wang, H.; Huang, H.-S.; Fujita, T.; Wu, K. C. W.; Chen, L.-C.; Yamauchi, Y.; Ariga, K. Nanoporous Carbons through Direct Carbonization of a Zeolitic Imidazolate Framework for Supercapacitor Electrodes. *Chem. Commun.* **2012**, *48*, 7259−7261.
(44) Cychosz, K. A.; Guillet-Nicolas, R.; Garcia-Martinez, J.; Thommes, M. Recent Advances in the Textural Characterization of Hierarchically Structured Nanoporous Materials. *Chem. Soc. Rev.* **2017**, *46*, 389−414.
(45) Liu, B.; Sun, C.; Chen, G. Molecular Simulation Studies of Separation of $CH_4/H_2$ Mixture in Metal-Organic Frameworks with Interpenetration and Mixed-Ligand. *Chem. Eng. Sci.* **2011**, *66*, 3012−3019.
(46) Wen, L.; Cheng, P.; Lin, W. Mixed-Motif Interpenetration and Cross-Linking of High-Connectivity Networks Led to Robust and Porous Metal−Organic Frameworks with High Has Uptake Capacities. *Chem. Sci.* **2012**, *3*, 2288−2292.
(47) Kim, H. K.; Yun, W. S.; Kim, M.-B.; Kim, J. Y.; Bae, Y.-S.; Lee, J.; Jeong, N. C. A Chemical Route to Activation of Open Metal Sites in the Copper-Based Metal−Organic Framework Materials HKUST-1 and Cu-MOF-2. *J. Am. Chem. Soc.* **2015**, *137*, 10009−10015.
(48) Lu, J.; Luo, M.; Lei, H.; Bao, X.; Li, C. Epoxidation of Propylene on NaCl-Modified VCe1-x Cux Oxide Catalysts with Direct Molecular Oxygen as the Oxidant. *J. Catal.* **2002**, *211*, 552−555.
(49) He, X.; Wang, W.-N. MOF-based Ternary Nanocomposites for Better $CO_2$ Photoreduction: Roles of Heterojunctions and Coordinatively Unsaturated Metal Sites. *J. Mater. Chem. A* **2018**, *6*, 932−940.


DOI: 10.1021/acs.cgd.8b01606
*Cryst. Growth Des.* 2019, 19, 1095−1102